

Empirical Sample Complexity of Neural Network Mixed State Reconstruction

Haimeng Zhao,^{1,2,3} Giuseppe Carleo,^{1,2} and Filippo Vicentini^{1,2,4,5}

¹*Institute of Physics, École Polytechnique Fédérale de Lausanne (EPFL), CH-1015 Lausanne, Switzerland*

²*Center for Quantum Science and Engineering, École Polytechnique Fédérale de Lausanne (EPFL), CH-1015 Lausanne, Switzerland*

³*Zhili College, Tsinghua University, Beijing 100084, China*

⁴*CPHT, CNRS, École polytechnique, Institut Polytechnique de Paris, 91120 Palaiseau, France*

⁵*Collège de France, Université PSL, 11 place Marcelin Berthelot, 75005 Paris, France*

(Dated: July 6, 2023)

Quantum state reconstruction using Neural Quantum States has been proposed as a viable tool to reduce quantum shot complexity in practical applications, and its advantage over competing techniques has been shown in numerical experiments focusing mainly on the noiseless case. In this work, we numerically investigate the performance of different quantum state reconstruction techniques for mixed states: the finite-temperature Ising model. We show how to systematically reduce the quantum resource requirement of the algorithms by applying variance reduction techniques. Then, we compare the two leading neural quantum state encodings of the state, namely, the Neural Density Operator and the positive operator-valued measurement representation, and illustrate their different performance as the mixedness of the target state varies. We find that certain encodings are more efficient in different regimes of mixedness and point out the need for designing more efficient encodings in terms of both classical and quantum resources.

I. INTRODUCTION

Recent advances in quantum technologies [1] have led to diversified applications in areas such as quantum simulation [2], communication [3], cryptography [4] and machine learning [5]. However, present-day *noisy intermediate-scale quantum* (NISQ) devices are inherently noisy [6] and limited in size. Techniques to mitigate noise [7], reduce quantum circuit depth [8], minimize the number of quantum shots, and verify experimentally prepared states [9] are crucial to leveraging these devices in realistic applications.

One such technique, quantum state reconstruction (or tomography) [10], uses a limited number of measurements to produce a classical approximation $\hat{\rho}$ of the quantum state ρ prepared on a device. The *classical reconstruction* facilitates the efficient computation of many observables without further quantum circuit evaluations and serves to validate the quantum device [9]. Classical reconstructions, which vary in computational overhead, are all derived from datasets of measurement outcomes collected by repeatedly measuring a set of observables on the state ρ prepared on the device. The accuracy of the reconstruction can be quantified via several *reconstruction errors* ϵ , such as the difference in expectation values between the reconstruction and the original state or other distance measures like infidelity or trace distance between $\hat{\rho}$ and ρ . An important indicator of the asymptotic performance of such methods is the sample complexity: the size of the *quantum-generated dataset* needed to obtain a classical reconstruction with a certain error ϵ .

Recent research has established that tomography methods using generic quantum states, such as maximum likelihood estimation [11, 12]), necessitate a sample size that grows exponentially with the system size [13–15]. One way to circumvent this is to design randomized mea-

surement protocols that only estimate expectation values of certain observables (e.g., classical shadow tomography [16–19]) Alternatively, one can exploit the fact that only a small set of possible states, with low complexity, are actually observed in physical models [20, 21], and design more efficient encodings of those physically realizable states to alleviate the data requirement, similar to variational methods commonly adopted to simulate quantum systems classically. For example, one can use matrix product states to efficiently encode and reconstruct one-dimensional pure states with area law entanglement [22, 23]. For more general states, generative neural networks (NN) can be used as a variational ansatz trained to reproduce the measurement data [24–29]. These ansätze, called Neural Quantum States (NQS), encode the quantum state in a compact form, significantly reducing the data requirement for reconstructions. The cost associated with this approach is introducing a non-convex optimization problem, which established techniques in modern artificial intelligence can approximately solve [30, 31].

Designing efficient NQS encodings for general mixed states presents a significant challenge. Three broad categories exist: (i) an expansion onto a set of pure-states encoded with standard NQS, which is exponentially costly for states with large entropy [32]; (ii) a physical (positive-semidefinite) neural-network encoding of the mixed state in the Pauli-Z computational basis known as Neural Density Operator (NDO) [29, 33] and (iii) a neural network encoding of the probability distribution over the outcomes of a set of informationally-complete positive operator-valued measurements (POVM-NQS). This last approach is less costly than (ii), but may result in unphysical density matrices [26–28, 34]. While the approximation used in the first approach is well-understood, the relationship between the latter two methods remains unclear. Furthermore, no comparison has been made thus

far regarding their effectiveness in Quantum State Reconstruction tasks. In particular, whether these two methods share the same sample complexity is uncertain.

While the dependence on system size has been extensively studied [27, 35], few comparisons have been made regarding the dependence on reconstruction error ϵ . This ϵ dependence can be especially significant for NISQ algorithms such as variational quantum eigensolvers (VQEs) [8, 36], as a worse scaling will lead to a large increase in the number of quantum executions to achieve the same accuracy of the result. For classical shadow tomography, the sample complexity is known to scale as ϵ^{-2} , which doesn't yield an asymptotic improvement over naive statistical averaging [17, 37]. More recently, numerical evidence suggests that the pure state NQS method holds an approximately quadratic advantage (i.e., ϵ^{-1}) over classical shadow in energy estimation for certain molecular ground states [38]. However, it is unknown if this advantage persists when the target state is mixed.

In this work, we first improve the reconstruction algorithm by considerably reducing its classical computational overhead using the Control-Variates variance reduction technique (section III).

Then, we conduct comprehensive numerical simulations to investigate the sample complexity of mixed-state reconstruction for different NQS encodings. In particular, we benchmark NDO and POVM-NQS on reconstructing the finite temperature density matrix of the Transverse-Field Ising model. We numerically demonstrate that for NDO, the quadratic advantage in pure state reconstruction can only survive when the state is slightly mixed, and the scaling deteriorates when the state is highly mixed. On the other hand, POVM-NQS does not hold such an advantage even for pure states and has a similar scaling as classical shadows, independent of how mixed the target state is. Consequently, NDO performs better than POVM-NQS for nearly pure states, while for highly mixed states, the situation is reversed. We also propose a phenomenological model that can explain the results. These results provide valuable guidance to the practical implementation of NQS-based state reconstruction and also point out the need for designing more efficient encodings in terms of quantum resources.

II. NEURAL QUANTUM STATE RECONSTRUCTION

We begin by describing the general framework of NQS reconstruction. The fundamental concept involves training a (potentially generative) NN that approximates a quantum state in a well-defined basis to reproduce the statistics of the measurement data. Let's assume that in the experiments, the system state ρ has been measured with N_b different POVM measurements $\{\{P_i^b\}_{i=1}^K\}_{b=1}^{N_b}$, where $\sum_{i=1}^K P_i^b = I$. This includes projective measurements like Pauli string measurements as a special case. Assume that we have gathered N_d measurement

outcomes under each measurement basis, where each outcome is denoted by a number $\sigma_j^b \in \{1, \dots, K\}$ for $j = 1, \dots, N_d$. The dataset that we aim to reproduce can be represented as:

$$D = \bigcup_{b=1}^{N_b} D_b = \bigcup_{b=1}^{N_b} \{\sigma_j^b\}_{j=1}^{N_d}. \quad (1)$$

We use $p_b(\sigma)$ to denote the probability of obtaining the measurement outcome σ by measuring ρ under basis b , and use $q_b^\theta(\sigma)$ to denote the corresponding probability given by the NQS ρ_θ with variational parameters θ . Our goal is to minimize the averaged distance between these two probability distributions over all bases. We quantify this distance by the Kullback–Leibler divergence $\text{KL}(p||q) = \mathbb{E}_{\sigma \sim p} \log \frac{p(\sigma)}{q(\sigma)}$. We, therefore, define the loss function as:

$$\begin{aligned} \mathcal{L}(\theta) &= \frac{1}{N_b} \sum_{b=1}^{N_b} \text{KL}(p_b || q_b^\theta) \\ &\approx \frac{1}{N_b} \sum_{b=1}^{N_b} \frac{1}{N_d} \sum_{j=1}^{N_d} \log q_b^\theta(\sigma_j^b) + \text{const.}, \end{aligned} \quad (2)$$

where we have omitted the constants that do not depend on θ and approximated the expectation values \mathbb{E} with the sample average over the finite dataset. We then use gradient-based optimization methods to optimize the parameters θ , in which the t^{th} iteration reads

$$\theta_t = \text{opt}(\theta_{t-1}, \nabla_\theta \mathcal{L}(\theta_{t-1})), \quad (3)$$

where opt refers to the optimization algorithm used (e.g, for gradient descent with learning rate α , $\text{opt}(\theta, g) = \theta - \alpha g$). In practice, when the dataset is large, we employ a technique called mini-batching to reduce the computational cost. This involves estimating the KL-divergence and its gradient not on the whole dataset, but only on a smaller subset of it. Once the training procedure has converged, the NQS can be used to generate samples, predict properties of interest, or, for sufficiently small systems, retrieve the full density matrix.

We now briefly introduce the two different NQS encodings that we compared during our investigations: NDO and POVM-NQS.

A. Neural Density Operator

The NDO encoding is compatible with projective measurements. We take Pauli string measurements $\{X, Y, Z\}^{\otimes N}$ on an N -qubit system as an example. The corresponding projectors will be denoted with $\{P_i^b\}$ and the basis rotation matrix with $\{U_b\}$. Measurement outcomes can be denoted by bit-strings of length N (e.g., $\sigma_j^b = (0100)$ for $N = 4$). When a properly normalized neural network (NN) is used - for instance, an autoregressive NN - to parameterize the density matrix elements

$\langle \eta | \rho_\theta | \eta' \rangle = \text{NN}_\theta(\eta, \eta')$, the variational probability distribution reads

$$q_b^\theta(\sigma) = \sum_{\eta, \eta'} \langle \sigma | U_b | \eta \rangle \langle \sigma | U_b | \eta' \rangle^* \text{NN}_\theta(\eta, \eta'). \quad (4)$$

If the NN parameterization is not normalized, an additional normalization term in the loss function appears, whose gradient can be estimated through Monte Carlo sampling [25]. Note that this method works for generic projective measurement schemes that may not be informationally complete.

B. POVM-NQS

The POVM-NQS method exploits the one-to-one correspondence between the state ρ and the outcome statistics of a single ($N_b = 1$) informationally complete POVM measurement $\{P_i\}_{i=1}^K$. The probability of obtaining an outcome $\sigma \in \{1, \dots, K\}$ is given by $p(\sigma) = \text{tr}(\rho P_\sigma)$. Conversely, the density matrix can be obtained by the inverse formula

$$\rho = \sum_{\sigma, \sigma'} p(\sigma') T_{\sigma\sigma'}^{-1} P_\sigma, \quad (5)$$

where $T_{\sigma, \sigma'} = \text{tr}(P_\sigma P_{\sigma'})$ is the overlap matrix [39]. Therefore, reconstructing $p(\sigma)$ suffices to determine ρ . As an example, we consider the tensor products of single-qubit Pauli-4 measurements $\{P_{(0),(1),(2)} = \frac{1}{3} |\uparrow_{x,y,z}\rangle \langle \uparrow_{x,y,z}|, P_{(3)} = I - P_{(0)} - P_{(1)} - P_{(2)}\}^{\otimes N}$ for an N qubit system. Under this measurement scheme, a normalized neural network is used to approximate $p(\sigma)$: $q^\theta(\sigma) = \text{NN}_\theta(\sigma)$. When the NN is trained, one can use the inverse formula to reconstruct the target state, or directly estimate relevant properties via sampling [27].

III. VARIANCE REDUCTION VIA CONTROL VARIATES

To investigate the asymptotic behavior of the sample complexity, we must train the NN to high precision. However, we observe that the noise introduced by the mini-batching strategy makes accurate training prohibitively expensive in practice. This becomes clear when we consider that, by randomly sampling a batch of outcomes B from the dataset at each iteration, the gradient is computed as:

$$g_B(\theta) = \frac{1}{|B|} \sum_{\sigma_j^b \in B} \nabla_\theta \log q_b^\theta(\sigma_j^b), \quad (6)$$

which is an unbiased estimator, with variance

$$\text{Var}[g_B] = \frac{1}{|B|} \text{Var}_{\{\sigma^b \sim p_b\}} \left[\frac{1}{N_b} \sum_{b=1}^{N_b} \log q_b^\theta(\sigma^b) \right], \quad (7)$$

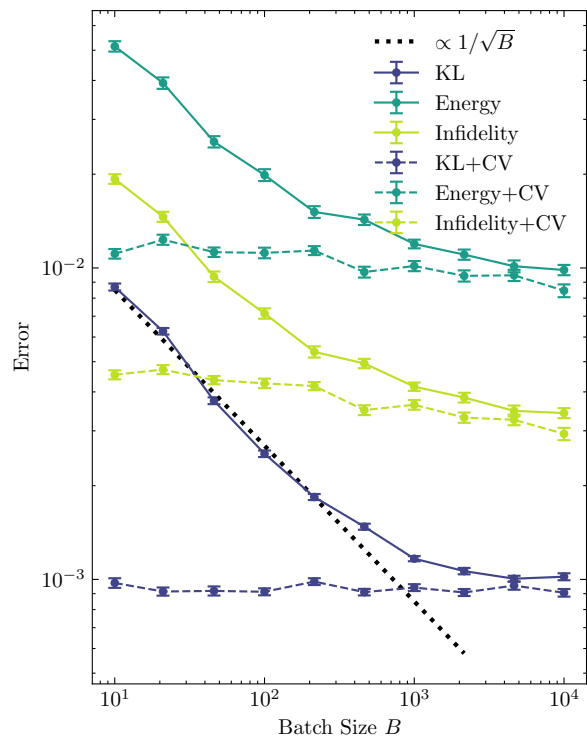


FIG. 1. NQS reconstruction of the ground state of 3-qubit 1D open-boundary transverse field Ising model using NDO with different batch sizes B . KL divergence, energy error and infidelity are used as metrics for performance. Dashed and solid lines represent the results of training with and without the control variates method. The dotted line marks the $1/\sqrt{B}$ scaling. All the data points are averaged over 100 random instances.

which remains finite as q_b^θ approaches the target p_b . This asymptotically finite variance is in sharp contrast to the zero-variance property of Variational Monte Carlo, which allows for accurate optimization of the ground-state with a relatively small number of samples [40, 41]. The statistical fluctuations in the gradient estimation introduce noise that prevents the reconstruction error from dropping below its standard deviation, which scales proportionally to $1/\sqrt{|B|}$. Consequently, in situations where we cannot afford training with large batch sizes, we must reduce the variance of the gradient estimator.

The Control Variates (CV) method is a well-established statistical technique for variance reduction [42], which was recently discussed in the context of Variational Monte Carlo [41, 43–45]. Specifically, when estimating the gradient $g_B(\theta_t)$ at step t , we introduce a second random variable (the CV), which represents the gradient evaluated at an earlier step t' : $g_B(\theta_{t'})$. We then adjust the gradient estimator to $g_B(\theta_{t-1}) - g_B(\theta_{t'}) + \mathbb{E}g_B(\theta_{t'})$. This revised estimator is unbiased but can have lower variance because $g_B(\theta_t)$ and $g_B(\theta_{t'})$ are correlated. The expectation can be computed by averaging over the entire dataset. Consequently, we obtain the following

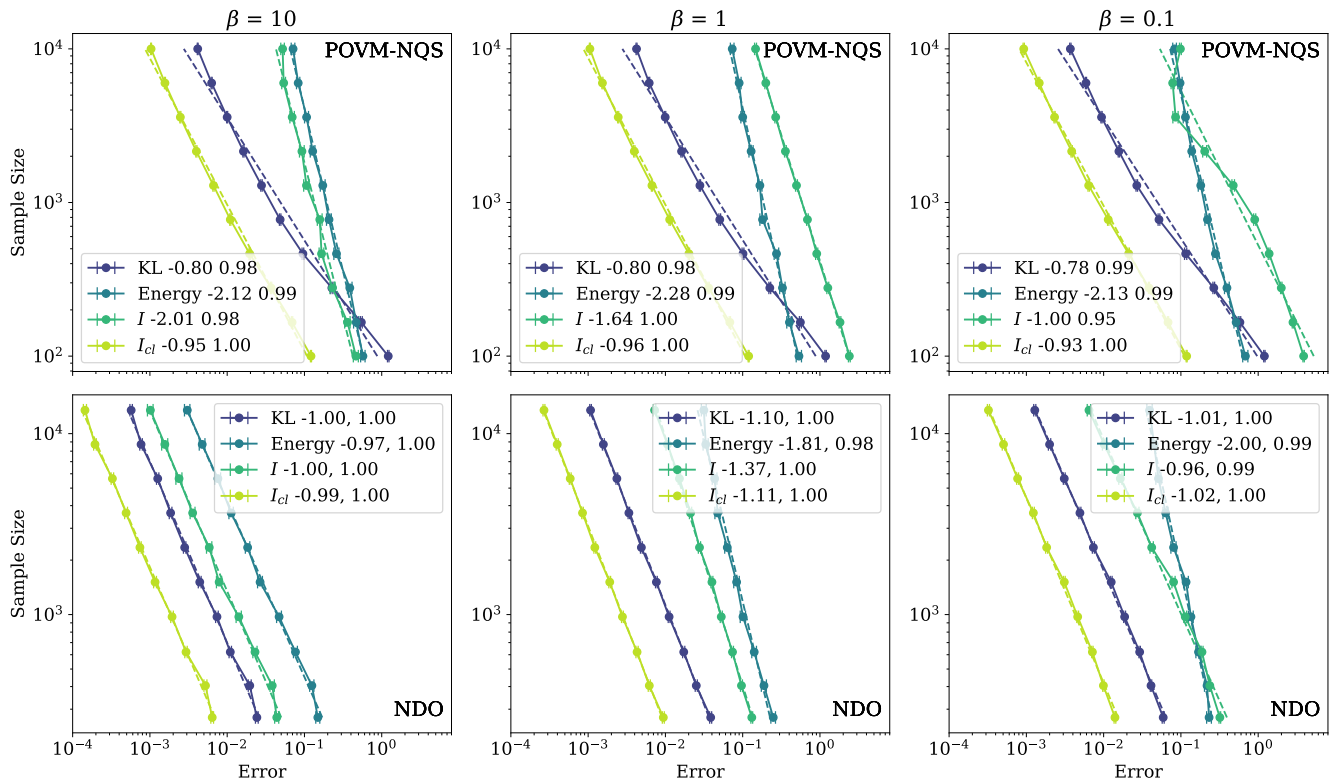


FIG. 2. Sample complexity dependence on the reconstruction error for 3-qubit 1D open-boundary transverse field Ising model under different inverse-temperature $\beta = 10, 1, 0.1$ using POVM-NQS (top) and NDO (bottom). KL divergence, energy error, infidelity and classical infidelity are used as metrics for reconstruction error. Dashed lines represent the log-log linear regression results, with the slopes and r^2 values indicated in the legend. All data points are averaged over 100 random instances.

variance-reduced training rule:

$$\theta_t = \text{opt}(\theta_{t-1}, g_B(\theta_{t-1}) - g_B(\theta_{t'}) + \nabla_{\theta} \mathcal{L}(\theta_{t'})). \quad (8)$$

To further reduce the computational cost, we update the CV only once every T steps, i.e., $t' = T \lfloor t/T \rfloor$. For all simulations in this paper, we set $T = 50$. This method is also known as *stochastic variance reduced gradient* (SVRG) in the machine learning literature [46, 47].

To further substantiate our approach, we conduct a systematic numerical analysis. As a benchmark problem, we consider the NDO reconstruction of the one-dimensional open-boundary transverse field Ising model (TFIM)

$$H_{\text{Ising}} = - \sum_{i=1}^{N-1} Z_i Z_{i+1} - h \sum_{i=1}^N X_i. \quad (9)$$

We set $h = 1$ and $N = 3$, small enough to study the batch size's effects systematically. We randomly generate 10^3 measurement shots for each of the $3^3 = 27$ Pauli basis, train the NQS with and without CV for different values of the batch size B , and repeat every simulation 100 times with different initial conditions and random seeds. In fig. 1, we compare three metrics, the KL divergence averaged over all measurement basis (KL), the

error in energy $\varepsilon = |\text{tr}(H\rho_{\theta}) - \text{tr}(H\rho)|$, and the infidelity $I(\rho, \rho_{\theta}) = 1 - (\text{tr} \sqrt{\sqrt{\rho_{\theta}} \rho \sqrt{\rho_{\theta}}})^2$. Dashed and solid lines correspond to training with and without CV. It is evident that when NQS is trained without CV, the errors scale like $1/\sqrt{B}$ as expected from eq. (7), and then saturates for large batch size at an intrinsic limit set by the dataset. When the CV method is applied, the adverse effect of mini-batching is eliminated, and the errors are independent of the batch size. These results validate the effectiveness of our CV method, which we will use in the rest of our analysis.

We note that this CV method applies to generic NQS reconstruction algorithms, including different pure and mixed encodings, and should be used as a default technique when mini-batching introduces noise. The code is implemented and open-sourced in NetKet [48–50].

IV. RESULTS AND DISCUSSION

A. Simulations

To study the performance of NDO and POVM-NQS, we simulate the finite-temperature Gibbs ensemble of the

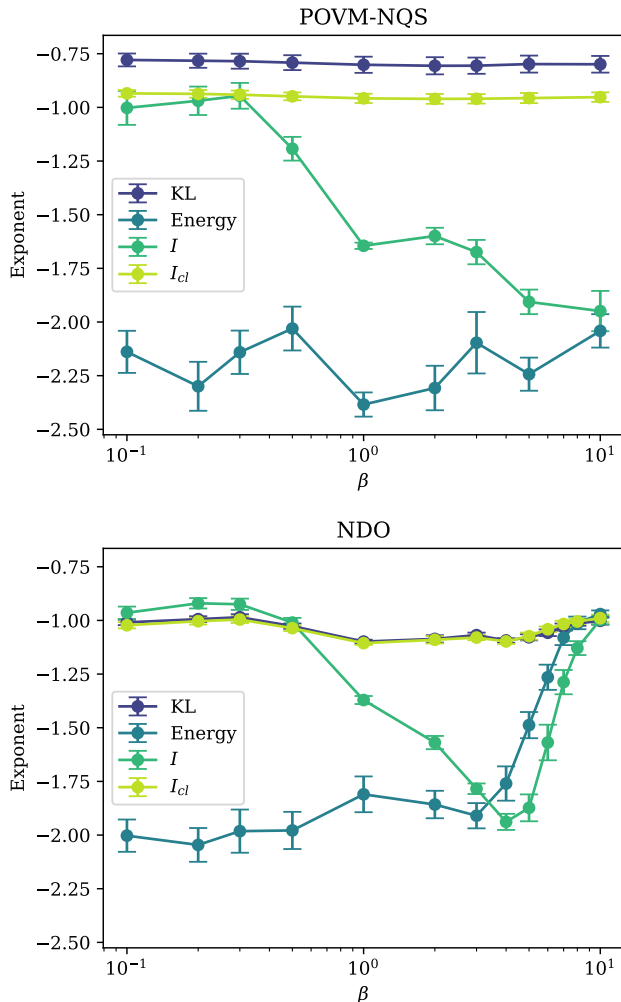


FIG. 3. The scaling exponents of reconstruction error for 3-qubit 1D open-boundary transverse field Ising model under different inverse-temperature $\beta \in [10^{-1}, 10^1]$ with POVM-NQS (top) and NDO (bottom). KL divergence, energy error, infidelity, and classical infidelity are used as metrics for reconstruction error. The error bars are given by linear regression.

TFIM, which is representative of mixed states where the prepared states might interact with a thermal bath.

We generate measurement datasets of varying sizes and use different NQS ansätze for the reconstruction to understand the asymptotic scaling behavior of the sample complexity. In this work, we focus on sample sizes in the regime of 10^2 to 10^4 , which are currently achievable with modern quantum devices [51, 52]. By plotting the errors of different sample sizes on a log-log scale, we can determine the sample complexity scaling exponents from the slopes of the linear fits. We use the loss value (defined in eq. (2)), the infidelity I , and the error in energy ε as metrics for the reconstruction error. As the density matrix reconstructed through the POVM-NQS method might be negative, the infidelity may not always be a

good indicator. Therefore, we take the absolute value of infidelity and also calculate the average classical infidelity $I_{cl} = 1 - \frac{1}{N_b} \sum_b \sum_{\sigma} \sqrt{p_b(\sigma) q_b^{\theta}(\sigma)}$, which is commonly used as a performance indicator in the literature on POVM-NQS.

We consider the 3-qubit one-dimensional open-boundary TFIM at $h = 1$, and use thermal states $\rho_{\beta} = \exp(-\beta H_{\text{Ising}}) / \text{tr}[\exp(-\beta H_{\text{Ising}})]$ across a wide range of inverse-temperatures $\beta \in [10^{-1}, 10^1]$ as the target states. The numerical details can be found in appendix A. In Fig. 2, we show three inverse-temperatures $\beta = 10, 1, 0.1$ representing low, medium, and high-temperature regimes, respectively. We plot the sample complexity scaling behaviors using solid lines, with the linear fits shown as dashed lines. The slopes and r-squared values of the linear fits are reported in the corresponding legends. In Fig. 3, we summarize the scaling exponents for different inverse temperatures.

B. Scaling Behavior

As shown in fig. 3, we note that the scaling exponents for KL and classical infidelity for both classes of NQS ansätze are approximately -1 , regardless of the mixedness of the target states. This is because we are learning the classical probability distributions of the measurement outcomes, which is known to have sample complexity $\Theta(\epsilon^{-1})$, for a classical error ϵ quantified by the KL or classical infidelity [53].

Regarding energy, POVM-NQS and NDO show qualitatively different behaviors. The scaling exponent for POVM-NQS remains around -2 irrespective of the mixedness of the target state, suggesting that the method doesn't improve the asymptotic quantum shot complexity over naive statistical averaging or classical shadows. On the other hand, NDO exhibits a scaling exponent of approximately -1 for slightly mixed states, although this exponent gradually deteriorates to -2 for highly mixed states. This suggests that NDO has an advantage over POVM-NQS when the target state is only slightly mixed, but the advantage disappears when the mixedness increases significantly. As NDO ansätze can naturally represent pure-states, this observation is consistent with the behavior of pure-state reconstruction, which was recently numerically also demonstrated to have an exponent of -1 (see Ref. [38]). We further note that NDO tends to be more accurate than POVM-NQS in terms of reconstruction error for the same sample size. Still, the classical optimization process is often harder to converge, leading to higher classical overhead. This might be related to variance problems arising from zeroes in the density matrix, similar to what was recently found for variational dynamics in Ref. [41].

In appendix D, we conduct the same study for a molecular ground-state (LiH) subject to depolarization and find a consistent picture as here.

Error	KL		I_{cl}		I		Energy	
β	0	∞	0	∞	0	∞	0	∞
Shadows	-1		-1		/		-2	
POVM-NQS								
NDO					valley	-2	-1	

TABLE I. Scaling exponents for KL, classical infidelity, infidelity, and energy error for TFIM under different β with different methods. Valley means -1 for $\beta \rightarrow 0, \infty$ while decreasing to -2 for the intermediate regime.

C. Theoretical Analysis

The previous section discussed the asymptotic quantum shot complexity for both KL and classical infidelity. Now, our focus shifts to examining the error scaling on the energy and quantum infidelity, intending to provide a theoretical explanation for the observed behavior. To this end, we consider a simple phenomenological model of errors occurring in NQS reconstructions. After the training procedure, we assume that the NQS does not perfectly encode the target state, but has a small error denoted as δ . We then derive asymptotic expressions to identify how this error affects various error metrics. The findings are summarized in table I.

For POVM-NQS, which directly encodes the probability distribution of POVM outcomes, we make the assumption that

$$q^\theta(\sigma) = p(\sigma) + \delta\Delta(\sigma) + o(\delta^2), \quad (10)$$

where $\sum_\sigma \Delta(\sigma) = 0$. This implies that the total variation distance TV, defined as $\sum_\sigma |p(\sigma) - q^\theta(\sigma)|/2$ is of order δ . Building upon the theory of classical distributions learning, we understand that the sample complexity scales as $\text{TV}^{-2} \sim \delta^{-2}$ [53]. Since the energy can be expressed as an expectation over the POVM distribution $\sum_\sigma p(\sigma)H_\sigma$, with $H_\sigma = \text{tr}(P_{\sigma'}H)T_{\sigma'\sigma}^{-1}$ [27], the error in energy is also of order δ . As a result, the energy error exhibits an exponent of -2 .

For NDO, which directly encodes the density matrix elements, we consider:

$$\rho_\theta = \rho + \delta\Delta + o(\delta^2), \quad (11)$$

where $\text{tr}\Delta = 0$. The trace distance TD, defined as $\|\rho^\theta - \rho\|_1/2$ will therefore be of order δ . According to the theory of quantum state learning, the sample complexity scales as $\text{TD}^{-2} \sim \delta^{-2}$ [14]. In appendix B, we prove that the energy error is of order δ^2 when ρ is a pure state, and of order δ otherwise. This distinction arises from the cancellation of terms of order δ when the state is pure, due to the wavefunction being an eigenstate of the Hamiltonian. However, such cancellation doesn't occur for mixed states or generic observables, leading to the observed scaling behavior: the energy has an exponent

of -1 for pure states, deteriorating to -2 as mixedness increases.

Furthermore, we show that KL is of order δ^2 and establish a general proposition that the trace distance can be upper bounded by the square root of the KL. This finding is consistent with the exponent of -1 for KL.

The behavior of quantum infidelity presents a more complex scenario. According to the theory of quantum state tomography [13–15], infidelity should exhibit an exponent of -1 , which agrees with the NDO simulations when mixedness is small or large. However, in the regime of intermediate mixedness, we observe a degradation of the infidelity exponent, forming a so-called *valley*. We explain this phenomenon in appendix C due to the misalignment between KL and infidelity, and we can reproduce a qualitatively consistent valley with random reconstruction error Δ in numerical simulations. The remaining quantitative discrepancies might arise from complicated interactions between the NN structure, training heuristics, and properties of the target states.

For POVM-NQS, we observe that a simple switch from $I(\rho, \rho_\theta)$ to $I(\rho_\theta, \rho)$ significantly alters the behavior, indicating the presence of several negative eigenvalues in ρ_θ . This suggests that the observed behavior is primarily caused by the unphysical nature of POVM-NQS reconstruction and is presented here for completeness.

V. CONCLUSIONS

In this paper, we systematically study the sample complexity of NQS mixed-state reconstruction and compare different NQS encodings, including NDO and POVM-NQS. To achieve accurate reconstruction, we introduce a strategy to systematically suppress the noise introduced by mini-batching based on Control-Variates. We provide theoretical arguments and numerical proof that this strategy leads to significantly better accuracy of reconstruction algorithms and has no trade-offs. Even though we only discuss the case of mixed-state reconstruction, it can also be applied to any scheme based on NQS. We also open-sourced a high-quality implementation in the quantum state reconstruction (QSR) driver of NetKet [48, 49].

We then present extensive numerical simulations for the finite-temperature TFIM, which is a prototypical example of realistic scenarios that experimentalists would encounter in quantum simulation experiments on NISQ devices. We find that NDO offers a quadratic advantage over POVM-NQS and classical shadows in the asymptotic sample complexity when the state is pure or almost pure. This advantage deteriorates and eventually vanishes when the target state becomes more mixed. On the other hand, POVM-NQS treats states of various mixedness on an equal footing and does not have such an advantage at all, regardless of the state's mixedness. Therefore, NDO is a more efficient tool for state reconstruction for slightly mixed states.

Our results establish asymptotic sample complexity as an important performance indicator for designing NQS architectures and showcase the advantages of enforcing physical constraints at the level of the NN architecture. Finally, this manuscript also provides a first comparison of the performance of the NDO and POVM-NQS encodings for mixed-states, which has otherwise not been investigated and might be of interest for developing variational methods to simulate finite-temperature and/or open quantum systems.

ACKNOWLEDGMENTS

We thank J. Carrasquilla for insightful discussions. We acknowledge the Tsinghua Astrophysics High-Performance Computing platform and SCITAS (EPFL) for providing computational and data storage resources.

-
- [1] M. A. Nielsen and I. L. Chuang, *Quantum Computation and Quantum Information* (Cambridge University Press, 2010).
- [2] I. M. Georgescu, S. Ashhab, and F. Nori, Quantum simulation, *Reviews of Modern Physics* **86**, 153 (2014).
- [3] N. Gisin and R. Thew, Quantum communication, *Nature photonics* **1**, 165 (2007).
- [4] N. Gisin, G. Ribordy, W. Tittel, and H. Zbinden, Quantum cryptography, *Reviews of modern physics* **74**, 145 (2002).
- [5] J. Biamonte, P. Wittek, N. Pancotti, P. Rebentrost, N. Wiebe, and S. Lloyd, Quantum machine learning, *Nature* **549**, 195 (2017).
- [6] J. Preskill, Quantum computing in the nisq era and beyond, *Quantum* **2**, 79 (2018).
- [7] Z. Cai, R. Babbush, S. C. Benjamin, S. Endo, W. J. Huggins, Y. Li, J. R. McClean, and T. E. O’Brien, Quantum error mitigation, *arXiv preprint arXiv:2210.00921* (2022).
- [8] J. R. McClean, J. Romero, R. Babbush, and A. Aspuru-Guzik, The theory of variational hybrid quantum-classical algorithms, *New Journal of Physics* **18**, 023023 (2016).
- [9] J. Carrasco, A. Elben, C. Kokail, B. Kraus, and P. Zoller, Theoretical and experimental perspectives of quantum verification, *PRX Quantum* **2**, 010102 (2021).
- [10] M. Paris and J. Rehacek, *Quantum state estimation*, Vol. 649 (Springer Science & Business Media, 2004).
- [11] A. I. Lvovsky, Iterative maximum-likelihood reconstruction in quantum homodyne tomography, *Journal of Optics B: Quantum and Semiclassical Optics* **6**, S556 (2004).
- [12] J. Řeháček, Z. Hradil, and M. Ježek, Iterative algorithm for reconstruction of entangled states, *Physical Review A* **63**, 040303 (2001).
- [13] S. T. Flammia, D. Gross, Y.-K. Liu, and J. Eisert, Quantum tomography via compressed sensing: error bounds, sample complexity and efficient estimators, *New Journal of Physics* **14**, 095022 (2012).
- [14] J. Haah, A. W. Harrow, Z. Ji, X. Wu, and N. Yu, Sample-optimal tomography of quantum states, in *Proceedings of the forty-eighth annual ACM symposium on Theory of Computing* (2016) pp. 913–925.
- [15] H. Yuen, An improved sample complexity lower bound for (fidelity) quantum state tomography, *Quantum* **7**, 890 (2023).
- [16] S. Aaronson, Shadow tomography of quantum states, in *Proceedings of the 50th annual ACM SIGACT symposium on theory of computing* (2018) pp. 325–338.
- [17] H.-Y. Huang, R. Kueng, and J. Preskill, Predicting many properties of a quantum system from very few measurements, *Nature Physics* **16**, 1050 (2020).
- [18] C. Hadfield, S. Bravyi, R. Raymond, and A. Mezzacapo, Measurements of quantum hamiltonians with locally-biased classical shadows, *Communications in Mathematical Physics* **391**, 951 (2022).
- [19] A. Elben, S. T. Flammia, H.-Y. Huang, R. Kueng, J. Preskill, B. Vermersch, and P. Zoller, The randomized measurement toolbox, *Nature Reviews Physics* **5**, 9 (2023).
- [20] F. G. Brandão, W. Chemissany, N. Hunter-Jones, R. Kueng, and J. Preskill, Models of quantum complexity growth, *PRX Quantum* **2**, 030316 (2021).
- [21] D. Poulin, A. Qarry, R. Somma, and F. Verstraete, Quantum simulation of time-dependent hamiltonians and the convenient illusion of hilbert space, *Physical review letters* **106**, 170501 (2011).
- [22] T. Baumgratz, A. Nüßeler, M. Cramer, and M. B. Plenio, A scalable maximum likelihood method for quantum state tomography, *New Journal of Physics* **15**, 125004 (2013).
- [23] B. Lanyon, C. Maier, M. Holzäpfel, T. Baumgratz, C. Hempel, P. Jurcevic, I. Dhand, A. Buyskikh, A. Daley, M. Cramer, *et al.*, Efficient tomography of a quantum many-body system, *Nature Physics* **13**, 1158 (2017).
- [24] G. Carleo and M. Troyer, Solving the quantum many-body problem with artificial neural networks, *Science* **355**, 602 (2017).
- [25] G. Torlai, G. Mazzola, J. Carrasquilla, M. Troyer, R. Melko, and G. Carleo, Neural-network quantum state tomography, *Nature Physics* **14**, 447 (2018).
- [26] J. Carrasquilla, G. Torlai, R. G. Melko, and L. Aolita, Reconstructing quantum states with generative models, *Nature Machine Intelligence* **1**, 155 (2019).
- [27] T. Schmale, M. Reh, and M. Gärttner, Efficient quantum state tomography with convolutional neural networks, *npj Quantum Information* **8**, 115 (2022).
- [28] P. Cha, P. Ginsparg, F. Wu, J. Carrasquilla, P. L. McMahon, and E.-A. Kim, Attention-based quantum tomography, *Machine Learning: Science and Technology* **3**, 01LT01 (2021).
- [29] G. Torlai and R. G. Melko, Latent space purification via neural density operators, *Physical review letters* **120**, 240503 (2018).
- [30] I. Goodfellow, Y. Bengio, and A. Courville, *Deep learning* (MIT press, 2016).
- [31] G. Torlai, G. Mazzola, G. Carleo, and A. Mezzacapo, Precise measurement of quantum observables with neural-network estimators, *Physical Review Research* **2**,

- 022060 (2020).
- [32] A. Melkani, C. Gneiting, and F. Nori, Eigenstate extraction with neural-network tomography, *Phys. Rev. A* **102**, 022412 (2020).
- [33] F. Vicentini, R. Rossi, and G. Carleo, Positive-definite parametrization of mixed quantum states with deep neural networks, arXiv preprint arXiv:2206.13488 (2022).
- [34] M. Neugebauer, L. Fischer, A. Jäger, S. Czischek, S. Jochim, M. Weidemüller, and M. Gärtner, Neural-network quantum state tomography in a two-qubit experiment, *Phys. Rev. A* **102**, 042604 (2020).
- [35] D. Sehayek, A. Golubeva, M. S. Albergo, B. Kulchitskiy, G. Torlai, and R. G. Melko, Learnability scaling of quantum states: Restricted boltzmann machines, *Physical Review B* **100**, 195125 (2019).
- [36] A. Kandala, A. Mezzacapo, K. Temme, M. Takita, M. Brink, J. M. Chow, and J. M. Gambetta, Hardware-efficient variational quantum eigensolver for small molecules and quantum magnets, *nature* **549**, 242 (2017).
- [37] J. M. Lukens, K. J. Law, and R. S. Bennink, A bayesian analysis of classical shadows, *npj Quantum Information* **7**, 113 (2021).
- [38] D. Iouchtchenko, J. F. Gonthier, A. Perdomo-Ortiz, and R. G. Melko, Neural network enhanced measurement efficiency for molecular groundstates, *Machine Learning: Science and Technology* **4**, 015016 (2023).
- [39] J. Carrasquilla, D. Luo, F. Pérez, A. Milsted, B. K. Clark, M. Volkovs, and L. Aolita, Probabilistic simulation of quantum circuits using a deep-learning architecture, *Physical Review A* **104**, 032610 (2021).
- [40] F. Becca and S. Sorella, *Quantum Monte Carlo approaches for correlated systems* (Cambridge University Press, 2017).
- [41] A. Sinibaldi, C. Giuliani, G. Carleo, and F. Vicentini, Unbiasing time-dependent variational monte carlo by projected quantum evolution (2023), arXiv:2305.14294.
- [42] P. P. Boyle, Options: A monte carlo approach, *Journal of financial economics* **4**, 323 (1977).
- [43] D. Wu, L. Wang, and P. Zhang, Solving Statistical Mechanics Using Variational Autoregressive Networks, *Physical Review Letters* **122**, 080602 (2019), publisher: American Physical Society.
- [44] O. Sharir, Y. Levine, N. Wies, G. Carleo, and A. Shashua, Deep Autoregressive Models for the Efficient Variational Simulation of Many-Body Quantum Systems, *Physical Review Letters* **124**, 020503 (2020), publisher: American Physical Society.
- [45] M. Hibat-Allah, M. Ganahl, L. E. Hayward, R. G. Melko, and J. Carrasquilla, Recurrent neural network wave functions, *Physical Review Research* **2**, 023358 (2020).
- [46] R. Johnson and T. Zhang, Accelerating stochastic gradient descent using predictive variance reduction, *Advances in neural information processing systems* **26** (2013).
- [47] S. Mohamed, M. Rosca, M. Figurnov, and A. Mnih, Monte carlo gradient estimation in machine learning, *The Journal of Machine Learning Research* **21**, 5183 (2020).
- [48] G. Carleo, K. Choo, D. Hofmann, J. E. T. Smith, T. Westerhout, F. Alet, E. J. Davis, S. Efthymiou, I. Glasser, S.-H. Lin, M. Mauri, G. Mazzola, C. B. Mendl, E. van Nieuwenburg, O. O'Reilly, H. Théveniaut, G. Torlai, F. Vicentini, and A. Wietek, Netket: A machine learning toolkit for many-body quantum systems, *SoftwareX* , 100311 (2019).
- [49] F. Vicentini, D. Hofmann, A. Szabó, D. Wu, C. Roth, C. Giuliani, G. Pescia, J. Nys, V. Vargas-Calderón, N. Astrakhantsev, and G. Carleo, NetKet 3: Machine Learning Toolbox for Many-Body Quantum Systems, *SciPost Phys. Codebases* , 7 (2022).
- [50] D. Häfner and F. Vicentini, mpi4jax: Zero-copy mpi communication of jax arrays, *Journal of Open Source Software* **6**, 3419 (2021).
- [51] F. Arute, K. Arya, R. Babbush, D. Bacon, J. C. Bardin, R. Barends, R. Biswas, S. Boixo, F. G. Brandao, D. A. Buell, *et al.*, Quantum supremacy using a programmable superconducting processor, *Nature* **574**, 505 (2019).
- [52] M. Endres, H. Bernien, A. Keesling, H. Levine, E. R. Anschuetz, A. Krajenbrink, C. Senko, V. Vuletic, M. Greiner, and M. D. Lukin, Atom-by-atom assembly of defect-free one-dimensional cold atom arrays, *Science* **354**, 1024 (2016).
- [53] C. L. Canonne, A short note on learning discrete distributions, arXiv preprint arXiv:2002.11457 (2020).
- [54] F. Vicentini, A. Biella, N. Regnault, and C. Ciuti, Variational neural-network ansatz for steady states in open quantum systems, *Physical review letters* **122**, 250503 (2019).
- [55] D. P. Kingma and J. Ba, Adam: A method for stochastic optimization, arXiv preprint arXiv:1412.6980 (2014).
- [56] J. Bradbury, R. Frostig, P. Hawkins, M. J. Johnson, C. Leary, D. Maclaurin, G. Necula, A. Paszke, J. VanderPlas, S. Wanderman-Milne, and Q. Zhang, JAX: composable transformations of Python+NumPy programs (2018).
- [57] T. M. Cover and J. A. Thomas, *Elements of information theory* (John Wiley & Sons, 1999).
- [58] H. Zhao, Non-iid quantum federated learning with one-shot communication complexity, *Quantum Machine Intelligence* **5**, 3 (2023).
- [59] J. Liu, Y. Tang, H. Zhao, X. Wang, F. Li, and J. Zhang, Cps attack detection under limited local information in cyber security: a multi-node multi-class classification ensemble approach, arXiv preprint arXiv:2209.00170 (2022).

Appendix A: Numerical Details

Here we list the numerical details of our studies. The NDO used in the simulations of an N -qubit system is a restricted Boltzmann machine with one layer of N hidden neurons and N ancillas [54]. The POVM-NQS is an autoregressive dense NN with 2 layers of 10 neurons [27]. All training are conducted via the Adam optimizer [55] with learning rate 10^{-3} , batch size 100, maximal iteration number 10^5 and CV update frequency $T = 50$. The training is terminated when the loss value stops decreasing for 2000 iterations. All code is implemented with NetKet [48–50] and JAX [56].

We note that the numerical study of the NDO scaling for mixed states is computationally more challenging than the case of pure states, such as Ref. [38]. This is because for pure states, measurements of all the Pauli strings in the Hamiltonian suffice to determine the state, while for mixed states they don't. Intuitively, when the pure state ansatz is trained to reproduce the probability

distributions of all Hamiltonian terms, it gives an energy approximating the true energy, which is the minimal energy. Then by the variational principle, the state also approximates the ground state. In contrast, for mixed states, one has to measure an informationally-complete set of bases (e.g., all the Pauli bases) to minimize the reconstruction error. This exponentially growing basis-set size makes numerical simulations for larger systems very challenging. Nevertheless, our theoretical analysis is independent of the system size and agrees with numerical simulations on small systems. Also, a relevant open question would be to investigate what is the effect of a truncated basis set on the reconstruction accuracy, which is relevant for experimental implementation.

Appendix B: Theoretical Details

For NDO, we assume $\rho_\theta = \rho + \delta\Delta + o(\delta^2)$, and we will omit $o(\delta^2)$ in derivations in this appendix. The error in energy reads $|\text{tr}(\rho_\theta H) - \text{tr}(\rho H)| = \delta|\text{tr}(\Delta H)| + o(\delta^2)$, which is in general of order δ . However, if the state is pure, i.e., $\rho = |\psi\rangle\langle\psi|$ and we assume $\rho_\theta = (|\psi\rangle + \delta|\Delta\rangle)(\langle\psi| + \delta\langle\Delta|)$, where $\langle\Delta|\psi\rangle = 0$. Then $\Delta = |\Delta\rangle\langle\psi| + |\psi\rangle\langle\Delta|$, and $\text{tr}(\Delta H) = 2\text{Re}\langle\Delta|H|\psi\rangle = 0$, because $|\psi\rangle$ is an eigenstate of H . Thus the error in energy is of order δ^2 for pure states.

Moreover, for KL, we have

$$q_b^\theta(\sigma) = \text{tr}((\rho + \delta\Delta)P_\sigma^b) = p_b(\sigma) + \delta\text{tr}(\Delta P_\sigma^b). \quad (\text{B1})$$

Thus $\text{KL}(p_b\|q_b^\theta) = -\sum_\sigma p_b(\sigma)\log\left(1 + \delta\frac{\text{tr}(\Delta P_\sigma^b)}{p_b(\sigma)}\right) = -\delta\text{tr}(\Delta\sum_\sigma P_\sigma^b) = o(\delta^2)$, where we have used $\sum_\sigma P_\sigma^b = I$ and $\text{tr}\Delta = 0$. Therefore $\text{KL} = \sum_{b=1}^{N_b} \text{KL}(p_b\|q_b^\theta)/N_b = o(\delta^2)$.

In fact, apart from the phenomenological model, we can also derive the quadratic relation between KL and trace distance via the following inequality, which is model-independent.

Proposition 1 (*Trace distance bounded by KL over all Pauli basis*). For two n -qubit states ρ and ρ' , let $\text{TD} = \|\rho - \rho'\|_1/2$ be the trace distance and use $\sigma_i \in \{I, X, Y, Z\}$ to denote Pauli operators. Define the KL over all Pauli basis as $\text{KL} = \sum_{i_1, \dots, i_n=0}^3 \text{KL}(p_{i_1, \dots, i_n}\|p'_{i_1, \dots, i_n})$, where p and p' denote the Bernoulli probability distributions given by the corresponding Pauli measurements and states. Then we have

$$\text{TD} \leq \frac{2^n}{\sqrt{2}} \sqrt{\text{KL}}. \quad (\text{B2})$$

To show this, note that all Pauli string operators form a complete basis of the space of Hermitian matrices. Therefore, we can decompose ρ as

$$\rho = \sum_{i_1, \dots, i_n=0}^3 C_{i_1, \dots, i_n} \sigma_{i_1} \otimes \dots \otimes \sigma_{i_n}. \quad (\text{B3})$$

The coefficients

$$C_{i_1, \dots, i_n} = \frac{1}{2^n} \text{tr}(\rho \sigma_{i_1} \otimes \dots \otimes \sigma_{i_n}) = \frac{1}{2^n} \mathbb{E}_{\sigma \sim p_{i_1, \dots, i_n}}[\sigma], \quad (\text{B4})$$

where p_{i_1, \dots, i_n} is the Bernoulli distribution given by ρ measured in the basis $\sigma_{i_1} \otimes \dots \otimes \sigma_{i_n}$. We use the same notations with primes to denote the corresponding quantities of ρ' . Then the trace distance can be bounded by the differences in coefficients as

$$\begin{aligned} \text{TD} &\leq \frac{1}{2} \sum_{i_1, \dots, i_n=0}^3 |C_{i_1, \dots, i_n} - C'_{i_1, \dots, i_n}| \|\sigma_{i_1} \otimes \dots \otimes \sigma_{i_n}\|_1 \\ &= \frac{1}{2} \sum_{i_1, \dots, i_n=0}^3 |C_{i_1, \dots, i_n} - C'_{i_1, \dots, i_n}| \cdot 2^n. \end{aligned} \quad (\text{B5})$$

On the other hand, the differences in coefficients can be bounded as

$$\begin{aligned} &|(C_{i_1, \dots, i_n} - C'_{i_1, \dots, i_n})| \\ &= \frac{1}{2^n} \left| \mathbb{E}_{\sigma \sim p_{i_1, \dots, i_n}}[\sigma] - \mathbb{E}_{\sigma \sim p'_{i_1, \dots, i_n}}[\sigma] \right| \\ &\leq \frac{1}{2^n} \sum_{\sigma \in \{\pm 1\}} |p_{i_1, \dots, i_n}(\sigma) - p'_{i_1, \dots, i_n}(\sigma)| \\ &\leq \frac{2}{2^n} \sqrt{\frac{1}{2} \text{KL}(p_{i_1, \dots, i_n}\|p'_{i_1, \dots, i_n})}, \end{aligned} \quad (\text{B6})$$

where the last inequality follows from Pinsker's inequality [57]. Therefore, we arrive at

$$\begin{aligned} \text{TD}(\rho, \rho') &\leq \sum_{i_1, \dots, i_n=0}^3 \sqrt{\frac{1}{2} \text{KL}(p_{i_1, \dots, i_n}\|p'_{i_1, \dots, i_n})} \\ &\leq \frac{2^n}{\sqrt{2}} \sqrt{\text{KL}}, \end{aligned} \quad (\text{B7})$$

where we have used the mean inequality. This proposition can also serve as a guarantee for training quantum density estimators in the context of quantum federated learning [58, 59].

Appendix C: The Valley Phenomenon

Here we aim to provide an explanation of the valley phenomenon observed in NDO: the exponent of infidelity is -1 for $\beta \rightarrow 0, \infty$, while decreasing to -2 for intermediate β .

We start from our phenomenological model and try to find a relationship between KL and infidelity. Since the behavior of KL is well understood, such a relationship would give us insights into how infidelity behaves. We consider the error matrix Δ to be drawn randomly as $\Delta = AA^\dagger / \text{tr}(AA^\dagger)$, where each entry of A follows the complex standard Gaussian distribution. Then we calculate the

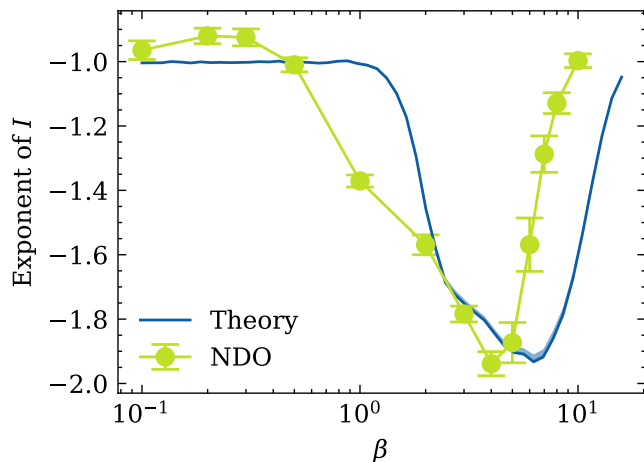


FIG. 4. The valley phenomenon in scaling exponents of infidelity for different β . The exponents observed in NDO simulations are plotted in orange, while the ones given by random perturbations are plotted in blue. Error bars and the shaded region indicate the standard deviation over 100 random instances.

perturbed state $\rho_\theta = \rho + \delta\Delta$, and normalize it again by dividing its trace.

For a given β and the corresponding target state ρ , we randomly generate 100 such perturbed states for different choices of $\delta \in [10^{-3.5}, 10^{-2.5}]$, and calculate the KL and infidelity I against the target state. We find that the resulting (KL, I) pairs fall on a straight line in log-log scale, with r -squared greater than 0.99. The slope $\alpha = \alpha(\beta)$ depends on β , and gives an effective power law relationship between KL and I : $I \propto \text{KL}^\alpha$. This means that the way we quantify the reconstruction error impacts the scaling exponents we observe. In particular, such misalignment between KL and infidelity leads to a β -dependent difference of $\alpha(\beta)$ in exponents.

Now we assume that KL has an exponent of -1 , which is theoretically and numerically validated. Hence the

sample complexity is proportional to $\text{KL}^{-1} \propto I^{-1/\alpha(\beta)}$. In fig. 4, we plot the simulated exponents $-1/\alpha(\beta)$ in blue, with the standard deviation indicated by the shaded region. We find a valley pattern that is qualitatively consistent with what we observe in NDO simulations, which confirms our theoretical explanation. The rest quantitative differences might be a complicated result of the NN design, generalization, training heuristics, and the property of the target states.

Appendix D: Depolarized Molecular Ground-states

In this appendix, we study the sample complexity scaling behavior for LiH ground-state subjected to depolarization noise. This scenario emerges in digital simulation or VQEs, where the quantum gates are imperfect and introduce noise that can be modeled as depolarization. We apply the parity transformation to transform the Fermionic Hamiltonian into a 4-qubit Hamiltonian that can be implemented on quantum computers (details of the transformations are found in the appendix of [25, 38]). We take its ground state $|\psi\rangle$ and simulate the depolarized states $\rho_p = (1-p)|\psi\rangle\langle\psi| + pI/2^4$ over $p \in [0, 1]$ as the target states. In fig. 5, we choose three depolarization intensity $p = 0, 0.01, 0.1$ that represents low, medium, and high depolarization regimes, and plot the corresponding results.

We observe that the behavior of POVM-NQS on LiH approximately matches what was seen on the TFIM, while the quantum shot complexity of the NDO is generally lower than that of TFIM by about 0.5. This might arise from the specific NN architecture and training heuristics used here. Intuitively, depolarization noise has less structure that can be exploited by NNs than thermal states, leading to a slightly worse scaling in the simulations. Nevertheless, an advantage of NDO over POVM-NQS can still be observed at small mixedness, while disappearing when decoherence leads to very mixed states, showing a consistent picture as TFIM.

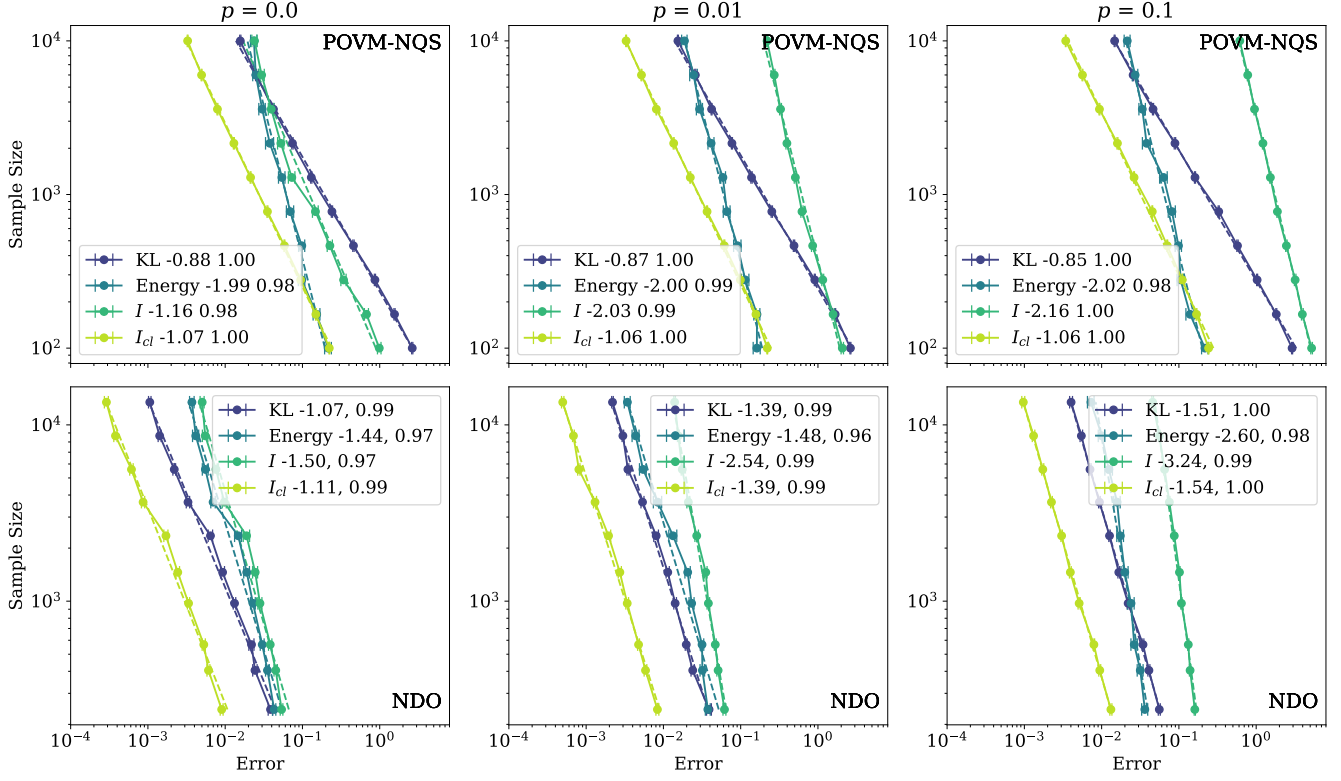


FIG. 5. Sample complexity dependence on the reconstruction error for LiH ground-state under different depolarization $p = 0, 0.01, 0.1$ using POVM-NQS (upper) and NDO (lower). KL divergence, energy error, infidelity and classical infidelity are used as metrics for reconstruction error. Dashed lines represent the log-log linear regression results, with the slopes and r^2 values indicated in the legend. All data points are averaged over 50 random instances.